Bioorg. Med. Chem. 76 (2022) 117097

Contents lists available at ScienceDirect

Bioorganic & Medicinal Chemistry

journal homepage: www.elsevier.com/locate/bmc

Radiolabelling Pt-based quadruplex DNA binders *via* click chemistry

Rainbow Lo [a,b], Aatikah Majid [b], Gilbert O. Fruhwirth [a,*], Ramon Vilar [b,*]

[a] Imaging Therapies and Cancer Group, Comprehensive Cancer Centre, School of Cancer and Pharmaceutical Sciences, King's College London, SE1 1UL London, UK
[b] Department of Chemistry, Molecular Sciences Research Hub, White City Campus, Imperial College London, W12 0BZ London, UK

A B S T R A C T

Guanine-rich sequences of DNA and RNA can fold into intramolecular tetra-helical assemblies known as G-quadruplexes (G4). Their formation *in vivo* has been associated to a range of biological functions and therefore they have been identified as potential drug targets. Consequently, a broad range of small molecules have been developed to target G4s. Amongst those are metal complexes with Schiff base ligands. Herein, we report the functionalisation of one of these well-established G4 DNA binders (based on a square planar platinum(II)-salphen complex) with two different radiolabelled complexes. An ^{111}In-conjugate was successfully used to assess its *in vivo* distribution in a mouse tumour model using single-photon emission computed tomography (SPECT) imaging. These studies highlighted the accumulation of this Pt-salphen-^{111}In conjugate in the tumour.

1. Introduction

Besides its canonical double stranded structure, DNA can fold into several other secondary structures. One of these, the guanine-quadruplex (G4) DNA, has attracted significant interest over the past two decades due to its proposed roles in telomere maintenance, gene expression and replication amongst others.[1–4] Because of these functions, G4s have also been studied as drug targets[1, 5-7] and therefore many molecules have been designed and developed to bind to this DNA structure.[8–10] The interactions between small molecules and G4s, have been studied using a broad range of spectroscopic and biophysical techniques such as melting assays (via fluorescence and UV/vis spectroscopy), circular dichroism (CD), structural characterisation (via X-ray crystallography and NMR spectroscopy) and surface plasmon resonance (SPR) amongst others.[11] Some of these molecules have been further studied *via* biochemical and cellular assays to establish whether their affinity to G4s is retained in a cellular environment leading to a biological function. A particularly attractive sub-class of G4 binders are luminescent molecules that change their optical properties (e.g. emission intensity or lifetime) upon DNA binding.[12–15] Such molecules have been widely studied using *in vitro* biophysical assays and, in some cases, have been investigated in cells providing valuable information of G4 formation and function.[16–18].

While most G4 binders were initially based on polyaromatic organic compounds, several metal complexes have also been shown to display excellent G4 binding capabilities.[19–20] Besides their structural role, the metal centre can confer unique properties (e.g. optical, catalytic, redox) to this type of compounds, which in turn can be very useful in studying quadruplexes. Metal complexes coordinated to Schiff bases (e.g. salphen L^1 – see Scheme 1) have been studied in depth as G4 DNA binders, with some of these complexes showing high affinity and selectivity for quadruplexes *in vitro* and a range of cellular effects.[21–31] In particular, square planar Pt^{II}-salphen complexes (see Scheme 1) possess a range of properties that makes them suitable as G4 optical probes and potential anticancer agents. For example, some of these complexes have been proposed to target the G4 sequence in the promoter region of the *c-Myc* oncogene and downregulate its expression.[23] Moreover, several Pt^{II}-salphen derivatives have been shown to be cytotoxic against a range of cancer cell lines,[32–33] including some examples where the compounds are phototoxic.[34] These complexes display a luminescent switch-on effect upon binding to G4 DNA, which has proven very useful in studying their interactions both *in vitro* and in cells.

In spite of these advances, currently, the evaluation and real-time distribution of G4 binders *in vivo* (i.e. in whole organisms rather than cell culture) has been limited to a handful of studies using whole-body fluorescence imaging.[35–36] The fundamental limitation of optical imaging *in vivo* is the lack of depth penetration, which leads to signal attenuation and increased photon scatter by tissues. In practice, while superficial tumours can be imaged successfully, deeply seated tumours are difficult to image due to increased photon scattering, resulting in a reduction in sensitivity and resolution.

Although imaging modalities that make use of radionuclide probes such as positron emission tomography (PET) or single-photon emission computed tomography (SPECT) do not present these issues, to the best of our knowledge, they have not been previously applied to study the *in vivo* distribution of G4 binders in whole organisms. We note that a recent

* Corresponding authors.
E-mail addresses: gilbert.fruhwirth@kcl.ac.uk (G.O. Fruhwirth), r.vilar@imperial.ac.uk (R. Vilar).

https://doi.org/10.1016/j.bmc.2022.117097
Received 22 August 2022; Received in revised form 19 October 2022; Accepted 8 November 2022
Available online 13 November 2022

paper reported the successful conjugation of a Pt-terpyridine G4 binder with NOTA-^{64}Cu as a chemo-radiotherapeutic agent with high *in vitro* activity against cancer cells.[37]

The purpose of the work herein presented was to utilise SPECT to assess the *in vivo* distribution of a G4-stabilising ligand, i.e. to visualise the whole-body distribution of our radiolabelled probe. To this aim, herein we report the synthesis of two new radiolabelled Pt^{II}-salphen complexes (**6** with ^{68}Ga; **7** with ^{111}In) and show that they retain the *in vitro* G4 DNA binding properties of the unsubstituted parent complex (**1**). We also present SPECT-CT imaging data (*in vivo* and *ex vivo*) of complex **7** in a mouse tumour model demonstrating the overall *in vivo* distribution of the compound, thereby also highlighting its accumulation in the tumour. It is important to point out that the scope of the SPECT-CT studies was not aimed at establishing G4 DNA binding interaction *in vivo*, but rather investigating the biodistribution and clearance of the new radiolabelled Pt^{II}-salphen-^{111}In complexes.

2. Results and discussion

2.1. Copper-free cycloaddition reaction for the synthesis of Pt^{II}-salphen-DOTA-^{111}In

Our new imaging probes contain a Pt^{II}-salphen complex (i.e. a G4 binder) tethered to 1,4,7,10-tetraazacyclododecane-1,4,7,10-tetraacetic acid (DOTA). The two components are connected *via* strain-promoted alkyne–azide cycloaddition (SPAAC) chemistry as shown in Scheme 1. In addition, a symmetrical, unmodified (without linker or DOTA) control complex (**1**) was synthesised for comparison (Scheme 1).

The Pt^{II}-salphen complex **3**, bearing an azide handle for click chemistry, was synthesised *via* transmetallation of the corresponding Zn^{II}-salphen complex **2** with $PtCl_2$. BCN-DOTA was then rapidly attached to **3** through SPAAC chemistry within 30 min. DOTA-modified Pt^{II}-salphen (**4**) was obtained with >95% purity, as characterised by HPLC and high-resolution mass spectrometry (HRMS) – see Figs. S20 and S21). The non-radioactive 'cold' reference compound **5** was prepared from the metallation of **4** with In^{III} respectively and characterised *via* HPLC and HRMS (see Fig. S22). Complexes **1**, **3** and **4** were fully characterised by ^{1}H, ^{13}C and ^{195}Pt NMR spectroscopy and ESI-MS, and their purity established by elemental analysis and/or LC-MS (Figs. S6-S10, and S13-S23). Radiolabelling of **4** with ^{68}Ga and ^{111}In to synthesise **6** and **7** is discussed below.

2.2. DNA binding of functionalised Pt^{II}-salphen complexes.

The DNA binding of unmodified complex **1** and the non-radioactive di-metal complex **5** was assessed by biophysical assays. Spectrofluorimetric titrations were carried out based on the well-establish emission switch-on effect that Pt^{II}-salphen complexes normally display upon binding to DNA,[23,30,32–33] In total, seven G4 DNA structures including parallel (*c-Myc* and *ckit-2*), hybrid (*bcl-2*, *htelo.K*), antiparallel (*htelo.Na*, *HRAS1*, *22CTA*) as well as duplex DNA (*ds26*) were tested (see Table S1 for sequences). The binding isotherms for the Pt^{II}-In^{III} complex **5** are shown in Figure 1A. The best binding (K_a ranging 10^6–10^7 M^{-1} was observed for *c–Myc*, *ckit-2* (both parallel) and *bcl-2* (mixed hybrid). In

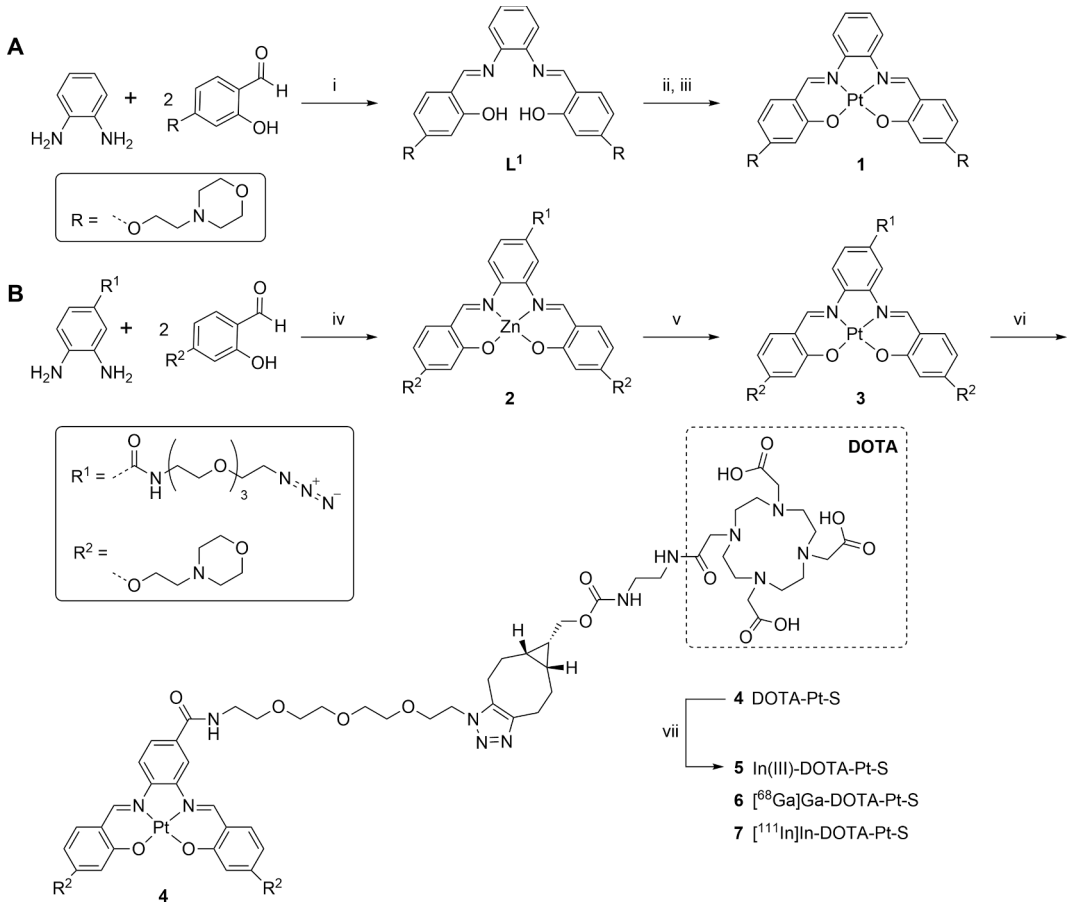

Scheme 1. Synthesis of A) platinum(II) salphen (**1**) and B) DOTA-functionalised platinum(II) salphen (**4**) complexes. Reagents and conditions: (i) MeOH, reflux, 12 h; (ii) NaOAc, MeCN, 60 °C, 10 min; (iii) K_2PtCl_4, DMSO, 6 h; (iv) $Zn(OAc)_2{\cdot}H_2O$, MeOH, reflux, 6 h; (v) $PtCl_2$, DMSO, 90 °C, 5 days; (vi) BCN-DOTA (BCN = Bicyclononyne, DOTA = dodecane tetraacetic acid), DMSO, RT, 2 h; (vii) Cold reference complex - $InCl_3{\cdot}x4H_2O$, radiolabelled complex – ^{68}Ga or ^{111}In, 0.2 M NaOAc buffer (pH 4.5), 90 °C, 30 min. RT = room temperature. All spectroscopic and analytical data for the characterisation of the compounds shown here can be found in the Electronic Supplementary Information (Figures S1–S23).

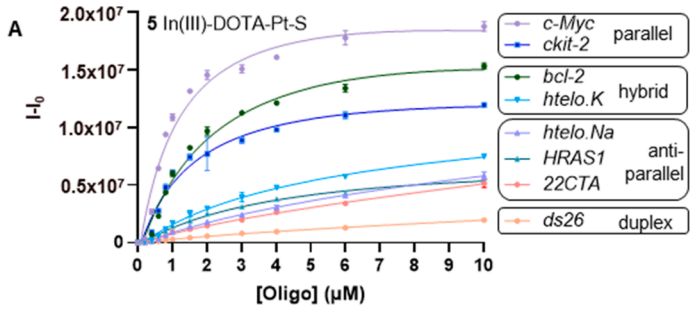

B

Oligo	1	5
c-Myc	1.41 ± 0.14 x 10^7	2.10 ± 0.27 x 10^7
ckit-2	7.15 ± 0.80 x 10^6	1.03 ± 0.15 x 10^7
bcl-2	6.19 ± 0.69 x 10^6	9.70 ± 0.96 x 10^6
htelo.K	2.20 ± 0.11 x 10^6	2.02 ± 0.18 x 10^6
htelo.Na	2.58 ± 0.30 x 10^6	9.61 ± 0.59 x 10^5
HRAS1	1.70 ± 0.13 x 10^6	1.96 ± 0.11 x 10^6
22CTA	2.80 ± 0.14 x 10^5	7.07 ± 0.83 x 10^5
ds26	n.d.	n.d.

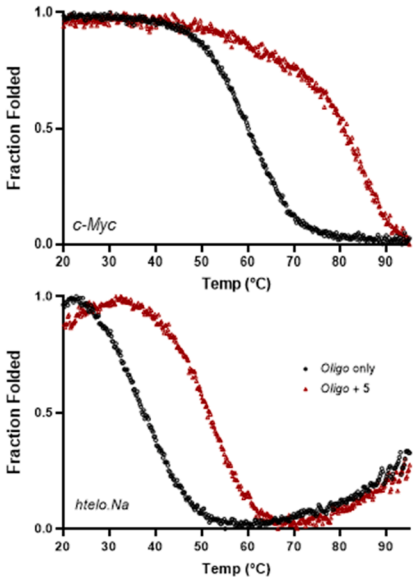

Figure 1. DNA binding experiments. Left: (A) Binding isotherms of complex **5** (2 μM) with a range of G4 structures including parallel (*c-Myc* and *ckit-2*), hybrid (*bcl-2*, *htelo.k*), antiparallel (*htelo.Na*, *HRAS1*, *22CTA*) and duplex (*ds26*) in the appropriate 10 mM LiCaco buffer, at pH 7.3. Oligonucleotide concentration 0.2–10 μM; λ_{ex} = 375 nm, λ_{ex} = 500–700 nm. (B) Summary of K_a values for **1** and **5** respectively. Right: CD melting spectra of G4 DNA (5 μM) in the presence of 25 μM complex **5** (red trace) in the appropriate 10 mM LiCaco buffer (pH 7.3; 1 mM KCl and 99 mM LiCl for *c-Myc* and 10 mM NaCl and 90 mM LiCl for *htelo.Na*). C) *c-Myc*, and D) *htelo.Na.* (For interpretation of the references to colour in this figure legend, the reader is referred to the web version of this article.)

contrast, binding to anti-parallel structures was less favourable (K_a ca. 10^5 M^{-1} and was worst for *ds26,* which could not be calculated due to its negligible interaction with **5**. A summary of K_a values for the parent Pt complex **1** and the Pt-In complex **5** is displayed in Figure 1B. This shows that all the Pt^{II}-salphen complexes investigated possessed similar binding profiles indicating there were minimal differences in DNA-binding between the unsubstituted complex (**1**) and the one modified with DOTA-In^{III} (**5**). It has been previously established that square-planar metal salphen complexes interact with G4 DNA via end-stacking. This binding mode allows for the metal centre (in this case platinum(II)) to be aligned with the potassium ions in the G4′s ion channel.[24] Considering the binding affinities and thermal stabilisation data for **1** and **5**, we would expect a similar binding mode for the platinum-salphen moiety of complex **5**.

Circular dichroism (CD) melting experiments were also conducted to confirm the G4 DNA binding properties of **5**; the studies were performed with *c-Myc* (parallel) and *htelo.Na* (anti-parallel) as representative examples of the two G4 DNA topologies. The melting curves shown in Figures 1C and 1D were obtained by recording the changes in ellipticity at 265 and 295 nm for *c-Myc* and *htelo.Na* respectively. From these melting curves, it can be seen that compound **5** induces thermal stabilisation for both structures, with ΔT_m values of 20.9 ± 0.6 °C and 13.6 ± 0.4 °C for *c-Myc* and *htelo.Na* respectively. This data corroborates results obtained from spectrofluorimetric titrations indicating that the novel di-metallic complex **5** is a good binder for G4s (particularly *c-Myc* DNA).

2.3. Synthesis of radiolabelled [^{68}Ga]- and [^{111}In]-DOTA-Pt-Salphen complexes.

Having established that attachment of the DOTA-In^{III} moieties to the Pt^{II}-salphen complex did not impact on G4 DNA binding properties, we proceeded to synthesise the radiolabelled derivatives. [^{68}Ga]Ga-DOTA-Pt-S (**6**) and [^{111}In]In-DOTA-Pt-S (**7**) were obtained by heating **4** to 90 °C with either $^{68}GaCl_3$ or $^{111}InCl_3$ in 0.2 M NaOAc buffer (pH 4.5) for 30 min. The radiochemical yields (RCY) were 96.5 ± 3.6 % and 97.4 ± 2.6 % for **6** and **7** respectively (mean ± SD, N = 3), as established by radio-HPLC (see Figs. S27–S29).

Free ^{68}Ga and ^{111}In eluted at *ca.* 2 min whereas the chelated product eluted at *ca.* 12 min. Heating **1** with either $^{68}GaCl_3$ or $^{111}InCl_3$ under the same conditions did not result in the formation of additional radiochromatogram peaks indicating the radiometal only interacted with the secondary chelator and not with Pt^{II}-salphen (see Figs. S30 and S31).

Sufficient radiotracer stability in serum is crucial as metal ion dissociation from its chelator, in presence of endogenous competitors (metal ions, ligands, proteins), could lead to accumulation in extraneous regions and hence is highly undesirable in cells and *in vivo*. Consequently, the stability of **6** and **7** in mouse serum was assessed over a period of 2 and 96 h respectively by radio-HPLC. Both radiolabelled complexes displayed excellent stability in mouse serum when incubated at 37 °C and showed no release of ^{68}Ga or ^{111}In over these time periods (see Fig. S27). The high RCYs (≥95%) of **6** and **7**, and the complex stability in mouse serum provided a good indication that radiometal and Pt^{II}-core were suitable for progression to *in vivo* studies. Compound **7** was chosen for further biological studies due to its longer half-life of ^{111}In compared to ^{68}Ga (2.1 d *vs.* 68 min), which allowed imaging over prolonged time.

2.4. In vivo biodistribution studies of complex 7.

In vivo distribution and clearance of **7** was studied by nanoSPECT/CT in a mouse melanoma tumour xenograft model at different time points over 72 h (see Figure 2A for an experimental scheme). Four B16-F10 tumour-bearing NOD.Cg-Prkdc^{scid} Il2rg^{tm1Wjl}/SzJ (NSG) were dosed with 4.3 ± 1.1 nmol of complex **7** (10.2 ± 2.5 MBq) in 75 μL of 0.2 M NaOAc buffer, pH 7.3. Prior to injection, the purity of **7** was assessed *via* radio-HPLC, then the solution was neutralised to pH 7.3 using 2 M NaOH and passed through a 0.2 μm sterile filter. The animals (n = 3) were sacrificed after the last imaging scan (72 h post-injection; *cf.* Figure 2A) and their organs harvested to provide radioactive compound **7** distribution across different organs/tissues (‘*ex vivo* biodistribution’) by gamma-counting.

Serial SPECT imaging was used with consecutive scans started at t = 0, 15 and 45 min as well as 72 h after initial compound administration (*cf.* Figure 2A). Using this approach, we obtained serial images each indicating the distribution of compound **7**, and when compared to one

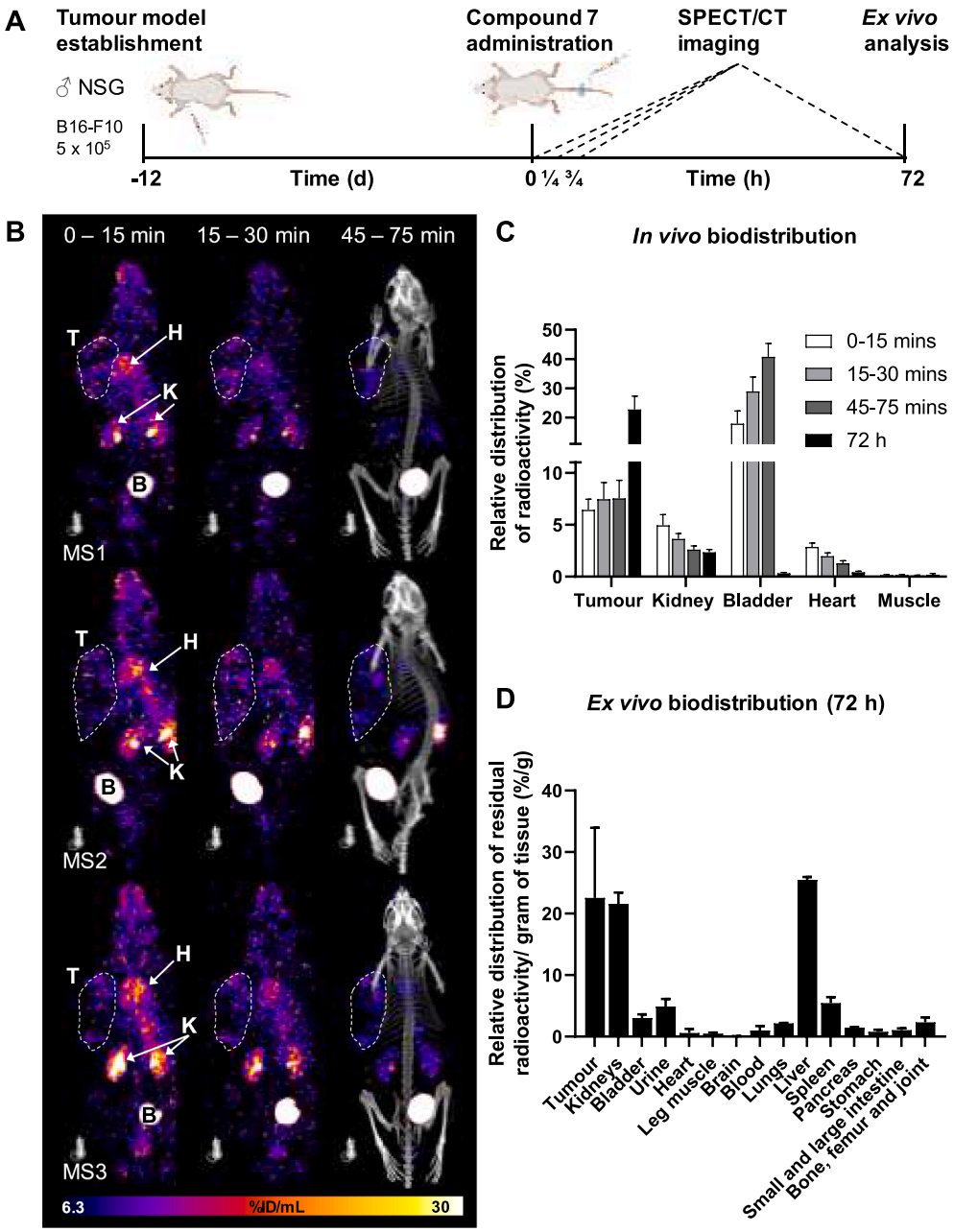

Figure 2. *In vivo* imaging of **7**. A) Experimental scheme. B) Maximum intensity projections (MIP) of SPECT only and overlayed SPECT/CT ad indicated time points after compound **7** administration (time ranges indicates duration of full SPECT scan). Tumour regions were segmented on CT scans and are highlighted as white dashed lines. Other regions of interest identified by arrows: kidneys (K), heart (H), bladder (B). C) Percentage distribution of radioactivity (%) in key ROIs, compared to the whole mouse, derived from image quantification from indicated images. D) Relative *ex vivo* distribution of residual radioactivity of **7** per gram of tissue in animals sacrificed 72 h after compound administration; mean ± SD of N = 3 animals. *Note:* the bladder and urine were recorded together for *in vivo* images and separately for *ex vivo* analysis.

another, reporting on changes in compound distribution within the same animal over time. Within the first 15 min after administration, radioactivity was detected in the blood pool as well as in the tumour, kidneys and the bladder (Figure 2C). Notably, over the course of the experiment, there was a reduction in radioactivity in the blood pool and other regions of interests (ROIs) such as thigh muscle. Concomitantly, there was an increase in radiotracer levels detected in the kidneys/bladder indicative of renal clearance. Images acquired over 30 min from t = 45 min revealed most of the radioactivity was cleared from the blood pool with the remaining radioactivity localised in the tumour, kidneys and bladder (Figure 2B-C). For all animals, there was clear evidence of compound **7** uptake in the tumour with radioactivity increasing from 6.4 ± 0.8 % of the administered dose at the first scan (t = 0–15 min) to 7.8 ± 1.6 % by the third scan (t = 45–75 min) (Figure 2B). In contrast, there was minimal activity in leg muscle over the same time span. Image quantification at 72 h indicated that the majority (99.4 ± 0.1%) of the administered radioactivity was excreted by this time point. Notably, 22.8 ± 3.7% of the remaining radioactivity at this late time point was concentrated in the tumour tissues (Figure 2D). This indicated that complex **7** remained preferentially localised to tumour tissues, although tumour uptake was heterogeneous. This is not unexpected for tumours of this cell line known to have necrotic cores (with little compound uptake) and dense intact tumour cell populations in their outer rims.[38]

In vivo imaging results were complemented by *ex vivo* gamma counting of radioactivity in harvested tissues 72 h after compound **7** administration (Figure 2D). The highest amount of radioactivity was found in liver, tumour and kidneys. Overall, our *in vivo* and *ex vivo* data indicated that compound **7** localized to tumours and remained there enriched compared to other tissues while excretion removed most of compound **7** from the animal within 72 h.

2.5. Cellular uptake studies via confocal microscopy.

Having carried out the *in vivo* biodistribution studies for complex **7**, it was of interest to establish whether this complex is cell permeable and hence could indeed target G4 DNA once localised in the tumour. To this

aim, we used the emissive properties of the Pt^{II}-salphen moiety in **5** (i.e. the non-radioactive analogue of **7**) to record confocal microscopy images in live U2OS, HeLa and HEK cells (the first two as representative examples of cancer cells while HEK was used as an example of non-cancerous cell line). This has been previously investigated with other Pt^{II}-salphen derivatives which have shown to be cell permeable and localise in the cell nucleus.[32] However, the new Pt-In complex **5** did not show to be cell permeable under the conditions used for this study (Fig. S32). To try and address this, we also performed cellular uptake studies by incubating cells with the probe in the presence of lipofectamine to permeabilise the cells. Unfortunately, this still showed very poor cellular uptake of our probe.

3. Conclusions

The primary objective of this work was to assess the feasibility of using nuclear imaging to visualise the *in vivo* distribution of a G4 binder. Importantly, we do not claim that we can image G4-binding in a whole-animal system, but rather the accumulation of the probe in specific tissues (including the tumour). We have demonstrated the use of copper-free click chemistry to functionalise a Pt^{II}-based G4 DNA binder with a second ligand suitable for the coordination of a second metal. This has been successfully used to synthesise the new Pt-Ga (**6**) and Pt-In (**7**) conjugates. *In vitro*, the conjugation of the DOTA-In^{III} complex had very little effect on the DNA binding properties of the Pt^{II}-salphen core. We demonstrated that the novel DOTA-conjugated Pt^{II}-salphen **4** could be radiolabelled with high RCY using $^{68}GaCl_3$ and $^{111}InCl_3$, and the resulting di-metallic complexes displayed excellent stabilities in mouse serum. We also assessed the *in vivo* distribution and clearance of the Pt^{II}-In^{III} complex **7** in a melanoma mouse model using SPECT/CT. Our results showed that **7** is rapidly cleared renally and is localised to the tumour site, with its presence in the tumours observed even 72 h after intravenous administration. In spite of the promising retention of the complex in the tumour, preliminary investigations show that the probe is not cell permeable and therefore retention in the tumour is not due to specific binding to intracellular targets (such as G4 DNA). While this limits the potential theranostic applications of this Pt-^{111}In conjugate, we show a successful route to functionalise a G4 DNA binder for whole body imaging *via* SPECT-CT. Further work will be aimed at developing systems that retain the cell permeability of the parent Pt^{II}-salphen complex. The imaging approach outlined in this work could be developed and validated further, to assess the suitability of novel G4-stabilising ligands for clinical translation, depending on effective tumour uptake, amongst other factors. Further, *in vivo* imaging, using nuclear modalities, could highlight potential areas of concern and assist the development of the next generation of G4-stabilising ligands.

4. Materials and methods

General experimental procedures

All commercial reagents, ligands and solvents were purchased and used without further purification from Sigma Aldrich, VWR, Fluorochem and Fisher Scientific, unless otherwise stated. Thin Layer Chromatography (TLC) was performed using Merck (Germany) aluminium-backed plated pre-coated with silica (0.2 mm, 60 F_{254}) and visualised at $\lambda = 254$ and 366 nm. Purification using column chromatography was performed with silica gel (Merck Kieselgel 60 F_{254} 320–400 mesh). ^{1}H NMR, ^{13}C NMR and ^{195}Pt NMR spectra were recorded on a Bruker Avance 400 MHz Ultrashield NMR, a Bruker DRX 500 MHz or a Bruker Ascend 500 MHz Fourier-transform NMR spectrometer, at 295 K unless otherwise stated. ^{195}Pt NMR were performed by Mr. Peter Haycock (Imperial College London). High resolution electrospray (ES) and Liquid Chromatography (LC-ES) mass spectra were obtained on a Waters LCT Premier (ES-Tof)/ACQUITY i-Class UPLC, fitted with a Waters BEH Acquity C18 50 mm × 2.1 mm column, by Dr Lisa Haigh (Imperial College London). The flow rate was 0.4 mL min^{-1}, with an injection volume of 10 μL. Solvent A: 99.9% Water, 0.1% formic acid. Solvent B: 99.9% acetonitrile, 0.1% formic acid. Solvent gradients started at 95% A and 5% B and changed to 5% A and 95% B by 3.2 min, before returning to the starting gradient (95% A, 5% B) by 3.5 min for a total run time of 4 min. Electrospray ionisation MS data was analysed using Waters LCT Premier. For accurate mass analysis, samples were referenced against Leucine Enkephalin at 557.2802 (M + H, C-13 isotope) and 556.2771 (M + H, C-12 isotope) positive mode, 555.2645 (M−H, C-13) and 554.2615 (M−H, C-12) negative mode. The maximum tolerated masses in HRMS were ± 5mDa. The software version MassLynx 4.1 (Waters Corporation, USA) was calibrated ignoring the electron in all cases. Data were recorded on a Lambda 25 UV–Vis spectrometer (Perkin Elmer, UK), using a 10 mm path-length quartz cuvette (Hellma, Müllheim, Germany). 1 mM ligand stocks in DMSO were diluted to 10 μM with 10 mM LiCaco buffer (pH 7.3). Spectra were acquired at room temperature between 200 and 700 nm and scanned at a speed of 240 nm/min. Emission spectra were recorded on a Cary Eclipse fluorescence spectrophotometer (Agilent Technologies, UK) using a 10 mm path-length quartz cuvette (Hellma, Müllheim, Germany). Parameters: λex = 370 nm and λem = 500–700 nm. Complex stock solutions were diluted from 1 mM DMSO ligand stocks to 10–20 μM, in 10 mM LiCaco at pH 7.3. All analysis was carried out using OriginPro (USA).

Elemental Analyses were performed by Mr. Alan Dickerson (University of Cambridge) using Exeter Analytical, Inc. CE-440 Elemental Analyzer, and run with a combustion temperature of 975 °C.

Non-radioactive analytical LC-MS spectra were obtained on a Waters HPLC system fitted with a Waters 515 HPLC pump, Waters 2767 autosampler, Waters XBridge C18 4.6 mm × 100 mm analytical column, Waters 3100 mass spectrometer and Waters 2998 photodiode array. Flow rate: 1.2 mL min^{-1}, injection volume 10 μL. Solvent gradients: mobile phase A was 5% MeCN in water and mobile phase B was acetonitrile 98% in water. The method used was a gradient increase using A to B over 18 min. All solvents contained additive (0.1% formic acid).

4.1. Preparation of oligonucleotide solutions

DNA oligonucleotides were purchased from Eurogentec (Belgium) in a lyophilised form. Oligo stock solutions were prepared using the appropriate buffer (see Table S1) according to the volumes recommended by the manufacturer. Oligo stock solution concentration were checked by measuring absorbance at 260 nm using a Perkin Elmer Lambda 25 spectrometer. The concentrations were calculated using the Beer-Lambert Law ($A = \varepsilon \bullet c \bullet l$, where ε is theoretical extinction coefficient, c is concentration of solution, l is pathlength). Stock solutions were annealed and stored at −20 °C until required. All oligos, except *c-Myc* were heated for 5 min at 95 °C and allowed to cool slowly over 2 h to room temperature. *c-Myc* was immediately placed in an ice bath for 30 min instead of slow cooling.

4.2. Synthesis of 2-hydroxy-4-(2-morpholinoethoxy) benzaldehyde

This compound was prepared using a modified version of a previously reported procedure.[39] 2,4-dihydroxybenzaldehyde (3.00 g, 22 mmol), 4-(2-chloroethyl)morpholine hydrochloride (4.05 g, 22 mmol) and sodium hydrogen carbonate (3.65 g, 42 mmol) were refluxed in acetone (120 mL) for 3 days at 68 °C under an inert atmosphere. After this time salts were filtered out and the solvent removed by reduced pressure. The crude residue was purified by flash chromatography (silica gel, eluent: cyclohexane/ethyl-acetate 90/10 v/v with 0.1% trimethylamine) yielding the product as an off-white solid (3.08 g, yield = 57%). ^{1}H NMR (400 MHz, DMSO-d_6): δ 11.04 (s, 1H; O*H*), 10.01 (s, 1H; C*H*O), 7.62 (d, $J = 8.7$ Hz, 1H; Ar*H*), 6.59 (dd, $J = 8.7$ Hz, $J = 2.3$ Hz, 1H; Ar*H*), 6.49 (d, $J = 2.3$ Hz, 1H; Ar*H*), 4.16 (t, $J = 5.7$ Hz, 2H; OCH_2), 3.58 (t, J = 4.4, 4H), 2.7 (t, $J = 5.7$ Hz, 2H; CH_2-N(CH_2)$_2$), 2.47 (t, $J = 4.4$ Hz, 4H; O-

$(CH_2)_2$-$(CH_2)_2$).

4.3. Synthesis of L^1

O-phenylenediamine (86.5 mg, 0.8 mmol) and 2-hydroxy-4-(2-morpholinoethoxy) benzaldehyde (402.0 mg, 1.6 mmol) were dissolved separately in MeOH (15 mL). Both solutions were combined slowly, forming a bright yellow solution, and the mixture was heated at 60 °C overnight. The yellow precipitate was collected and recrystallized from MeOH with slow diffusion of diethyl ether to yield the product as a bright yellow solid (359.5 mg, 78%). ^{1}H NMR (400 MHz, DMSO-d_6): δ 13.49 (s, 2H; –O*H*), 8.83 (s, 2H; C*H* = N), 7.53 (dd, J = 8.4 *J* = 3.2 Hz, 2H; Ar*H*), 7.48 (d, *J* = 9.1 Hz, 2H; Ar*H*), 7.35 (dd, J = 5.5, *J* = 3.6 Hz, 2H; Ar*H*), 6.55 (d, *J* = 7.7 Hz, 2H; Ar*H*), 6.49 (d, J = 8.9, 2H; Ar*H*), 4.19–4.10 (m, 4H; OCH_2), 3.62 – 3.54 (m, 8H;), 2.74–2.65 (m, *J* = 5.6 Hz, 7H; NCH_2); peak partially obscured by solvent peak, 2.68 – 2.65 (m, 1H) Last proton not seen, likely to be under the solvent peak. ^{13}CNMR (101 MHz, DMSO- *d6*): δ 163.9, 163.5, 163.3, 142.2, 134.5, 127.7, 120.0, 113.7, 107.7, 101.8, 66.6, 66.1, 57.3, 56.5, 54.1. ES(+)-MS *m/z* calculated for ($C_{32}H_{38}N_4O_6^+$): 575.2865; found: 575.2880 a.m.u. corresponding to $[M-H]^+$.

4.4. Synthesis of compound **1**

Ligand $\mathbf{L^1}$ (138 mg, 0.24 mmol) and sodium acetate (44.3 mg, 0.54 mmol) were dissolved in 19 mL acetonitrile and heated to 60 °C for 10 min. Upon dropwise addition of a DMSO solution (1 mL) of K_2PtCl_4, the reaction mixture turned from yellow to orange. After 24 h a bright orange precipitate had formed which was collected and washed with acetonitrile, water and diethyl ether and then dried under high vacuum (137 mg, yield = 74%). ^{1}H NMR (400 MHz, DMSO-d_6): δ 9.32 (s, 2H; C*H* = N), 8.36 (dd, J = 6.4 *J* = 3.4 Hz, 2H; Ar*H*), 7.74 (d, *J* = 9.1 Hz, 2H; Ar*H*), 7.38 (dd, J = 6.3, *J* = 3.2 Hz, 2H; Ar*H*), 6.60 (d, *J* = 2.4 Hz, 2H; Ar*H*), 6.47 (dd, J = 8.9, *J* = 2.4 Hz, 2H; Ar*H*), 4.18 (t, *J* = 5.6 Hz, 4H; OCH_2), 3.62 – 3.56 (m, 8H;), 2.73 (t, *J* = 5.6 Hz, 4H; NCH_2), 2.68 – 2.65 (m, 1H) Last proton not seen, likely to be under the solvent peak. ^{13}C NMR (126 MHz, DMSO-d_6) δ 166.5, 164.7, 149.6, 144.4, 136.8, 127.1, 116.6, 116.3, 108.2, 102.7, 66.2, 65.6, 56. 8, 53.6. ^{195}Pt NMR (500 MHz, DMSO-d_6) δ: −1759 ppm. ES(+)-MS *m/z* calculated for ($C_{32}H_{37}N_4O_6Pt^+$): 768.2, $C_{32}H_{38}N_4O_6Pt^{2+}$: 385, found: 768 a.m.u. corresponding to $[M]^+$ and 385 to $[M-2H]^{2+}$. Calc. %CHN for ($C_{32}H_{36}N_4O_6Pt$): %C 50.1, %H 4.7, %N 7.3. Found: %C 50.0, %H 4.6, % N 7.1.

4.5. Synthesis of 3,4-diamino-N-(2-(2-(2-(2-azidoethoxy)ethoxy) ethoxy)ethyl)benzamide

3,4-Diaminobenzoic acid (200 mg, 1.31 mmol) was dissolved in N, N'-dimethylformamide (15 mL) to yield a pale orange solution. To this stirring solution at room temperature, 1-hydroxybenzotriazole monohydrate (267 mg, 1.97 mmol), triethylamine (0.37 mL, 2.63 mmol) and 1-ethyl-3-(3-dimethylaminopropyl)carbodiimide (306 mg, 1.97 mmol) were added and stirred for 30 min under an inert atmosphere. Subsequently 11-azido-3,6,9-trioxaundecan-1-amine (Tokyo Chemical Industry, UK, 0.456 mL, 2.30 mmol) in N,N′–dimethylformamide (2 mL) was slowly dropped into the stirring solution, which was left under nitrogen for 12 h and heated to 45 °C. The solvent was removed under reduced pressure and purified *via* flash chromatography (silica gel, DCM/MeOH 95/5 v/v). The solvent was removed to yield a pink oil (282.2 mg, 61%). ^{1}H NMR (400 MHz, MeO*D*) δ 7.18 (d, *J* = 2.1 Hz, 1H, Ar*H*), 7.12 (dd, *J* = 8.1, 2.1 Hz, 1H, Ar*H*), 6.67 (d, *J* = 8.2 Hz, 1H, Ar*H*), 3.70–3.58 (m, 12H, multiple CH_2 from ethoxy linker), 3.52 (t, *J* = 5.5 Hz, 2H, amide-CH_2), 3.33 (d, *J* = 5.2 Hz, 2H, azide-CH_2). ESI(+)-MS *m/z* calcd for ($C_{15}H_{25}N_6O_4^+$): 353; found 353 a.m.u. corresponding to $[M + H]^+$.

4.6. Synthesis of compound **2**

Zinc acetate $Zn(OAc)_2{\cdot}H_2O$ (87.3 mg, 0.40 mmol) dissolved in 5 mL methanol was added dropwise to a solution of 2-hydroxy-4-(2-morpholinoethoxy)benzaldehyde (181.7 mg, 0.72 mmol) and 3,4-diamino-N-(2-(2-(2-(2-azidoethoxy)ethoxy)ethoxy)ethyl)benzamide (127.4 mg, 0.36 mmol) in 20 mL methanol yielding a bright yellow solution. The mixture was refluxed for 6 h under an inert atmosphere yielding a solid which was filtered and washed with different solvents (EtOAc, DCM and Et_2O). The product was isolated as a bright yellow precipitate (204.7 mg, yield = 64%). ^{1}H NMR (400 MHz, DMSO-d_6) δ 8.92 (d, *J* = 8.8 Hz, 2H, imine), 8.59 (t, *J* = 5.6 Hz, 1H, amide N*H*), 8.23 (d, *J* = 1.9 Hz, 1H, Ar*H*), 7.94–7.72 (m, 2H, Ar*H*), 7.31 (dd, *J* = 8.7, 5.1 Hz, 2H, Ar*H*), 6.30–6.12 (m, 4H, Ar*H*), 4.10 (s, 4H, CH_2), 3.64–3.33 (m, 25H, linker CH_2 over lapping signals), 2.70 (t, *J* = 5.6 Hz, 4H, CH_2), 2.47 (d, *J* = 4.2 Hz, 7H, morph CH_2 partially obscured by solvent peak). ^{13}C NMR (101 MHz, DMSO-d_6): δ 175.2, 174.9, 166.2, 165.0, 164.7, 162.3, 161.7, 142.1, 139.5, 138.1, 137.9, 132.2, 125.6, 116.2, 115.3, 114.8, 114.7, 105.3, 105.1, 104.8, 70.3, 70.2, 69.7, 69.5, 66.6, 65.6, 57.4, 54.1, 50.5, 39.5. ESI(+)-MS *m/z* calc. for ($C_{41}H_{53}N_8O_{10}Zn^+$): 882; found 882 $[M]^+$. Elemental analysis calc. %CHN for ($C_{41}H_{52}N_8O_{10}Zn{\cdot}3H_2O$) 52.6; H, 6.2; N, 12.0. Found C, 52.1; H 5.8; N, 11.6.

4.7. Synthesis of compound **3**

A DMSO (1 mL) solution of platinum(II) chloride (50.5 mg, 0.19 mmol) was added dropwise to compound **2** (167.6 mg, 0.19 mmol) in 4 mL DMSO to yield a yellow solution which was heated to 90 °C under an inert atmosphere. The progress of the reaction was monitored *via* TLC (silica gel, DCM/MeOH 9:1 v/v). When complete, the resulting dark red reaction mixture was purified by flash chromatography (silica, DCM/MeOH). The solvent was removed under reduced pressure and the product isolated as a bright orange solid (68.3 mg, yield = 36 %). ^{1}H NMR (400 MHz, C*D*Cl_3) δ 9.31 (d, *J* = 4.1 Hz, 2H, imine), 8.77 (s, 1H, amine N*H*), 8.69 (t, *J* = 5.5 Hz, 1H, Ar*H*), 8.38 (d, *J* = 8.9 Hz, 1H, Ar*H*), 7.82 (d, *J* = 9.4 Hz, 1H, Ar*H*), 7.79 – 7.68 (m, 2H, Ar*H*), 6.58 (s, 2H Ar*H*), 6.48 (t, *J* = 2.5 Hz, 1H, Ar*H*), 6.45 (t, *J* = 2.6 Hz, 1H, Ar*H*), 4.18 (t, *J* = 5.5 Hz, 4H, CH_2), 3.58 (dt, *J* = 14.0, 4.8 Hz, 16H, CH_2), 3.53 (s, 4H), 3.49 (q, *J* = 5.7 Hz, 3H), 2.73 (t, *J* = 5.5 Hz, 4H, CH_2). Aliphatic groups overlapping and partially obscured by solvent peak. ^{13}C NMR (101 MHz, DMSO-d_6): δ 166.78, 166.6, 165.1, 164.9, 164.8, 150.2, 149.8, 146.3, 144.1, 136.8, 132.5, 125.5, 116.7, 116.5, 115.8, 115.3, 108.6, 108.4, 102.6, 69.8, 69.7, 69.2, 69.0, 66.2, 65.6, 56.8, 56.1, 53.6, 39.9. ^{195}Pt NMR (86 MHz, DMSO-d_6): δ −1732.65 ppm. ES(+)-MS *m/z* calculated for ($C_{41}H_{53}N_8O_{10}Pt^+$): 1012.4, ($C_{41}H_{54}N_8O_{10}Pt^{2+}$): 507, found 1013 a.m.u. $[M + H]^+$, 507 a.m.u. $[M + 2H]^{2+}$. Elemental analysis calc. %CHN for ($C_{41}H_{52}N_8O_{10}Pt$): C 48.7, H 5.2, N 11.1. Found: C, 48.7; H, 5.3; N, 11.0.

4.8. Synthesis of compound **4**

Stock solutions of compound **3** and BCN-DOTA (CheMatech, France) were prepared in biological grade DMSO in Eppendorf tubes and were gently vortexed to ensure the solids had fully dissolved. These were BCN-DOTA (10.2 mg, 0.01 mmol) in 400 μL DMSO, and **3** (6.7 mg, 0.007 mol) in 536 μL DMSO. For the copper-free click reaction, 320 μL (0.004 mmol) of the solution of **3** and 96 μL (0.004 mmol) the solution of BCN-DOTA were added to an Eppendorf vial and agitated for 2 h at room temperature. The purity was determined *via* LC-MS (full conversion, 95% purity, see general experimental procedures for non-radioactive analytical LC-MS protocol) and used without further purification. ^{1}H NMR (400 MHz, DMSO-d_6) δ 9.35 (d, *J* = 6.5 Hz, 2H, imine), 8.80 (broad s, 1H, amide N*H*), 8.74 (s, 1H, Ar*H*), 8.41 (d, *J* = 9.2 Hz, 1H, Ar*H*), 8.17 (broad s, 1H, amide N*H*), 7.84 (d, *J* = 9.8 Hz, 1H, Ar*H*), 7.77 (d, *J* = 26.4 Hz, 2H, Ar*H*), 7.53 (broad s, 1H, amide N*H*), 6.61 (t, *J* = 2.0 Hz, 2H, Ar*H*), 6.48 (dt, *J* = 8.9, 2.9 Hz, 2H, Ar*H*), 4.34 (t, *J* = 5.1 Hz, 2H, CH_2),

4.19 (t, $J = 5.7$ Hz, 4H, CH_2), 3.98 (d, $J = 10.8$ Hz, 2H, CH_2), 3.69 (t, $J = 5.4$ Hz, 2H, CH_2), 3.63–3.54 (m, 8H, CH_2), 3.54–3.51 (m, 2H, CH_2), 3.48 (d, $J = 5.4$ Hz, 6H, CH_2), 3.41 (s, 4H, CH_2), 3.13 (s, 4H, CH_2), 3.06 (s, 2H, CH_2), 2.98 (s, 4H, CH_2), 2.93 (s, 4H, CH_2), 2.73 (s, 4H, CH_2), 2.67 (t, $J = 1.9$ Hz, 1H, CH), 2.60 (s, 2H, CH_2), 2.05 (s, 2H, CH_2), 1.51 (s, 2H, CH_2), 1.23 (s, 1H, BCN CH), 1.11–0.98 (m, 1H, BCN CH), 0.86 (s, 2H, CH_2). Note: there are several overlapping signals in the aliphatic region. In addition, this area is dominated by solvent peaks obscuring some of the signals making the assignment difficult (Figure S16). ^{13}C NMR (126 MHz, DMSO-d_6): δ 170.9, 167.1, 166.9, 165.5, 164.2, 164.2, 156.95, 151.2, 150.8, 146.7, 144.6, 143.5, 137.7, 134.2, 133.3, 117.7, 116.4, 108.7, 103.8, 99.5, 72.5, 70.3, 70.2, 70.2, 70.1, 69.8, 69.3, 64.3, 62.2, 61.6, 53.6, 52.0, 50.7, 47.6, 29.1, 25.9, 22.7, 22.3, 21.6, 21.3, 20.0, 19.5, 19.0, 18.1, 17.7. ^{195}Pt NMR (500 MHz, DMSO-d_6) δ: −1739.34 ppm. ES(+)-MS *m/z* calcd for ($C_{70}H_{99}N_{14}O_{19}Pt^+$): 1635, ($C_{70}H_{100}N_{14}O_{19}Pt^{2+}$): 818, found: 1634 $[M + H]^+$ and 818 a.m.u. $[M + 2H]^{2+}$. HRMS (ESI(+)/Q-TOF) *m/z*: Calcd for ($C_{70}H_{99}N_{14}O_{19}^{195}Pt^+$): 1634.6851, found 1634.6859 a.m.u. corresponding to $[M + H]^+$.

4.9. Synthesis of compound 5

Compound **4** (300 μL of a 1.8 mM stock, 0.54 mmol) and 730 μL 0.2 M NaOAc buffer (pH 4.5) were added to an Eppendorf vial and gently vortexed. $InCl_3{\cdot}x4H_2O$ (31 μL of a 17.2 mM stock in NaOAc buffer, 0.54 mmol) was added to the reaction vial and thoroughly mixed. After the pH was checked with pH strips (Whatman, Cytiva, USA), the reaction vessel was sealed tightly with PTFE tape and heated at 90 °C for 30 min, then allowed to cool to room temperature, and the pH was checked again. Aliquots were kept at −20 °C until use. The purity was determined *via* LC-MS (92% purity) and used without further purification. HRMS (ESI(+)/Q-TOF) mass spectrum of **5**, mass calculated for ($C_{70}H_{97}N_{14}O_{19}PtIn^+$): 1747.5741, found 1747.5720 a.m.u. corresponding to $[M + H]^+$.

See below for the synthesis of radioactive compounds **6** and **7**.

4.10. DNA binding experiments

Ligand preparation: Complex **1** was dissolved in DMSO or, in the case for compound **5**, as a DMSO-0.2 M NaOAc buffer mixture and kept at −20 °C until use. For DNA binding assays, stock solutions were further diluted to yield 1 mM stock solutions, which were aliquoted into separate Eppendorf tubes and stored at −20 °C until required, to avoid freeze–thaw cycles.

Emission titrations: Experiments were performed using a Clariostar Microplate reader (BMG Labtech, Germany), $\lambda_{ex} = 370$ nm and $\lambda_{em} =$ 500–700 nm, in addition to a matrix scan at 580 nm in Greiner Bio-One half volume (100 μL/well) plates. Ligand concentration was kept constant at 2 μM and the following DNA equivalents were tested: 0, 0.1, 0.2, 0.3, 0.4, 0.5, 0.75, 1, 1.5, 2, 3 and 5 in the appropriate buffer (see Table S1) at pH 7.3. Sample preparation was carried out by preparing working solutions of double concentration ligand (4 μM) and DNA in the appropriate buffer, before 50 μL of ligand and DNA were added to the appropriate well and mixed thoroughly. Experiments were conducted in triplicate and plotted in in GraphPad Prism 8 (GraphPad Software, USA). Binding constants (K_a) were calculated using the area under the curve, for each spectrum, and based on the methods detailed by Stootman *et al.* (2006) and Thordarson (2010).[40–41].

Circular Dichroism melting experiments: CD spectra were recorded on a Jasco J-715CD spectrometer (Jasco, Easton, USA) scanning from 320 to 220 nm with a pitch of 0.1 nm, at 100 nm•min^{-1}. Each CD trace was the average of 3 accumulations. Spectra were smoothed using the Savitzky-Golay filter, baseline corrected for corresponding blank buffer and plotted. Spectra were acquired from 20 to 95 °C (pitch = 0.2 °C), with additional data points acquired in peaks of interest (265 and 295 nm for *c-Myc* and *htelo.Na* respectively). Samples were recorded in a 10 mm path length quartz cuvette (Hellma, Müllheim, Germany) and all analysis was carried out using OriginPro. Samples were prepared using 5 μM oligonucleotide, annealed in 10 mM LiCaco buffer supplemented with either 1 mM KCl or 10 mM NaCl for *c-Myc* and *htelo.Na* respectively. Samples were subsequently mixed with increasing amounts of ligand up to 5 equivalents. Melting temperature (T_m) was determined by normalising the ellipticity (*mdeg*) between 0 and 1 and taking the temperature at which the normalized *mdeg* was 0.5.

4.11. Radiochemistry

Buffers and reagents were prepared in metal-free conditions, and handled using plasticware including spatulas, where possible. All reactions were carried out using 0.2 M NaOAc buffer (pH 4.5) in Eppendorf vials. Neutralisation of $^{68}GaCl_3$ and $^{111}InCl_3$ eluents were carried out using 0.2 M NaOAc buffer (pH 4.5) and 2 M NaOH respectively. MilliQ water was treated using Chelex 100 resin for a minimum of 3 days to remove any potential competing metal contaminants. The pH was monitored before and after heating using pH stipes. Radioactive analytical HPLC was performed by Rainbow Lo using a reversed-phase HPLC coupled to a UV detector and LabLogic Flow-Count radioactivity detector, with an Agilent Eclipse XDB-C18 column (4.6 × 150 mm, 5 μm). UV detection was set at 230 nm and radioactivity detector with a sodium iodide probe (B-FC-3200). The optimal method was a gradient increase of acetonitrile from 5% to 95% over the course of 30 min, with a flow rate of 1 mL•min^{-1}. Sample injection volume was 10 – 20 μL depending on the radioactivity as not to saturate the detector. Mobile phase A was water and mobile phase B was acetonitrile, both containing 0.1% TFA.

4.12. Synthesis of 6 and 7

$^{68}GaCl_3$ was eluted from an Eckert & Ziegler (E&Z, Berlin, Germany) generator using 5 mL clinical grade 0.1 M HCl (E&Z) in five 1 mL fractions. The activity of each fraction was measured by a Capintec (Mirion Technologies, USA) radionuclide dose calibrator. The highest activity fraction was selected for radiolabelling. $^{111}InCl_3$ was supplied by the Radiopharmacy Unit at Guy's and St Thomas's Hospital (London, UK). [^{68}Ga]Ga-DOTA-Pt-S (**6**) and [^{111}In]In-DOTA-Pt-S (**7**) were synthesised by heating **4** with either $^{68}GaCl_3$ or $^{111}InCl_3$ at 90 °C, in NaOAc buffer at pH 4.5, for 30 min. 2 M NaOH solution was used to adjust the pH accordingly. The pH was checked before and after heating. Quality control pertaining to evaluating the purity *via* radio HPLC, absorbance and monitoring the appearance of the solution (colour and solubility) was performed to ensure this was successful. For *in vivo* experiments, pH of sample solution was adjusted to pH 7 and syringe filtered (0.2 μm pore size). By adjusting the pH, free ^{111}In was converted to insoluble hydroxides that were removed before radiotracer injection.

4.13. Serum stability of 6 and 7

The stabilities of [^{68}Ga]Ga-DOTA-Pt-S, **6** and [^{111}In]In-DOTA-Pt-S, **7** were tested in PBS and mouse serum over several time points (endpoints 2 and 96 h respectively). After radiolabelling and confirmation of the desired products *via* radio-HPLC, the radiotracers were added to vials containing mouse serum (or PBS as a control) and incubated at 37 °C. The stabilities of these compounds were assessed as described below at time points 0, 30 60 and 120 min for the gallium analogue and 0, 1, 24, 48, 72 and 96 h for the indium analogue. Two measurements were taken at each time point: first, the radiotracer/serum mixture was gently vortexed and injected directly into the HPLC; second, ice cold ethanol was added to the samples, which were subsequently cooled on wet ice to precipitate most serum proteins followed by centrifugation to pellet the latter. Resultant supernatants were collected and analysed by HPLC.

4.14. Animal experimentation

All experimental protocols were monitored and approved by the King's College London Animal Welfare and Ethical Review Body Animal Welfare and Ethical Review Panel, in accordance with UK Home Office regulations (Project License 70/8879) under the Animals (Scientific Procedures) Act 1986 and UK National Cancer Research Institute (NCRI) Guidelines for the Welfare and Use of Animals in Cancer Research.

Animals. Young adult (5–6 weeks old, 24 ± 1 g) male NOD.Cg-Prkdc^{scid} Il2rg^{tm1Wjl}/SzJ mice (NSG; purchased from Charles River UK) were used for all animal experiments. All mice were maintained within the King's College London Biological Services Unit under specific pathogen-free conditions in a dedicated and licensed air-conditioned animal room (at 23 ± 2 °C and 40–60% relative humidity) under light/dark cycles lasting 12 h every day. They were kept in individually ventilated standard plastic cages (501 cm^2 floor space; from Tecniplast) including environmental enrichment and bedding material in the form of sterilized wood chips, paper strips and one cardboard roll per cage. Maximum cage occupancy was five animals, and animals were moved to fresh cages with fresh environmental enrichment and bedding material twice per week. Sterilized tap water and food were available *ad libitum*; food was PicoLab Rodent Diet 20 (LabDiet, USA) in the form of 2.5x1.6x1.0 cm oval pellets that were supplied at the top of the cages. Sentinel animals were kept on the same IVC racks as experimental animals and confirmed to be healthy after completion of the studies. In total, six animals were used.

Tumour model. B16-F10 murine melanoma cells were used to establish tumours in mice. Therefore, melanoma cells were washed with pre-warmed Hank's buffered saline without Ca^{2+} and Mg^{2+} (HBSS), re-suspended in HBSS and counted. Aliquots of 5x10^5 cells in 50 μL HBSS were injected intradermally on the left flank of the mice. Once palpable, tumour volumes were measured with callipers using the formula $V = \pi / 6 \cdot L \cdot W \cdot D$, wherein L is length, W is width and D is depth of the palpable tumour. Tumour volumes were determined by qualified staff using callipers at least every second day throughout the study. An aliquot of the injection cell suspension was re-plated in culture media after inoculation of animals to check melanoma cell viability of the batch after the administration procedure (and assessed on the next day by microscopy for adherence to the vessel and viability using the trypan blue method). The mice were injected with the radiotracer 11 days after tumour induction.

Radiotracer. [^{111}In]In-DOTA-Pt-S, (**7**) was intravenously administered into tumour-bearing animals at the beginning of the imaging experiment (t = 0). Therefore, 4.3 ± 1.1 nmol complex **7** in 75 μL (PBS, 0.2 M NaOAc buffer, neutralised to pH 7.3 using 2 M NaOH) under sterile conditions (equivalent dose administered with respect to mouse was 0.26 mg/kg).

***In vivo* radionuclide imaging.** Mice were anaesthetised using isoflurane (1.5% (v/v) in O_2). Protective eye gel was applied, and animals were left sedated and placed onto the imaging platform of a nanoSPECT-CT Silver upgrade scanner (Mediso, Hungary). After administration of **7**, animals were imaged using three consecutive SPECT scans (0–15, 15–30 and 45–75 min; 1.0 mm collimators) only interrupted for one CT scan (30–42 min at 55kVp tube voltage, 1200 ms exposure time, 360 projections) to provide anatomical context. Notably, 2 h after administration of **7**, one animal from the radiotracer group was euthanised to provide a snapshot of radiotracer uptake at this early time point. In addition, both animals from the saline control group were culled at this time point. All other animals that had received **7** were re-imaged by SPECT-CT 72 h after compound administration (SPECT: 40 min scan using 1.0 mm collimators; CT: 12 min scan as described above).

4.15. In vivo image analysis.

All SPECT-CT data sets were reconstructed using a Monte Carlo based full 3D iterative algorithm (Tera-Tomo, Mediso, Hungary). Decay correction to time of injection was applied. All images were analysed using VivoQuant software (inviCRO, USA), which enabled the definition of regions of interest (ROIs) in co-registered SPECT/CT images for quantification of radioactivity (SPECT) in tissues of interest. The total activity in the whole animal (excluding the tail) at time zero was defined as the injected dose (ID). ROIs for different organs were defined to express uptake in each organ as a percentage of injected dose per volume (%ID/mL), and relative percentage radioactivity (%) compared to the whole mouse. VivoQuant software and its implementation of Otsu's thresholding[42] was used to background-correct SPECT signals. To accurately monitor the change of radiotracer uptake over time, serially acquired scans were analysed in the same manner with identical co-registration offset parameters, voxel sizes and ROIs. ROIs were manually delineated using the CT image only, in each 2D slice over three views (coronal, sagittal and transverse). One set of ROIs were drawn for each mouse and applied to the other images in the same scanning session (i.e. the ROIs for a given animal at 0 – 15 mins, 15 – 30 mins and 45–75 mins after compounds administration all have the same voxel sizes and identical positions and volumes for the ROIs to enable quantification of radiotracer distribution over time). ROIs were redrawn on the second scanning day.

4.16. Analysis of radioactivity in harvested tissues.

For terminal *ex vivo* γ–counting, animals were euthanized after the 72 h imaging time point unless otherwise indicated. All harvested tissues were weighed, immediately immersed in 3.7% (w/v) formaldehyde solution, γ–counted using a 1480 Wizard 3 gamma–counter (Wallac, PerkinElmer, USA) alongside radioactivity calibration standards for ^{111}In. Relative percentage residual activity per gram of tissue (%/g) were calculated for each sample. Tissues were frozen and re-counted on different days, depending on the remaining activity as some organs contained too much activity and saturated the γ-counter detector (hence the samples were allowed to decay and were subsequently re-counted). Decay correction was performed relative to the time of initial compound administration.

4.17. Confocal imaging.

Fluorescence confocal microscopy were performed on a TCSPC SP5 II Confocal Microscope (Leica Microsystems GmbH, Germany). Live cell imaging was performed using a 100x magnification (numerical aperture (NA) 1.4) HCX PL APO CS oil immersion objective to collect the images at 512 × 512-pixel resolution. The excitation wavelengths were 458 nm for bright field and 380 nm for Hoechst-33342 and ligand (760 nm multi photon Coherent chameleon). Emission bandwidths were 400 nm–480 nm for Hoechst-33342 and 570 nm–700 nm for the ligand. Images were analysed in LAS X software.

U2OS cells were seeded at 2.0 × 10^4, HEK cells were seeded at 8.0 × 10^4 and HeLa were seeded at 6.0 × 10^4 in high glucose DMEM (10% FBS, L-glut and P/S, Gibco) in an 8-well plate (Lab-Tek, ThermoFischer, UK) and allowed to grow for 24 h each. The media was removed, and the cells were washed with PBS (Sigma). Probe **5** was diluted in DMEM and added to the cells with a total volume per well of 250 μL. After incubating for 24 h, the media was removed, and the cells were washed before addition of DMEM containing co-staining dye Hoechst 33,342 (4 μM). At this point cells were imaged as described above.

Declaration of Competing Interest

The authors declare that they have no known competing financial interests or personal relationships that could have appeared to influence the work reported in this paper.

Data availability

Data will be made available on request.

Acknowledgements

RL and AM were supported by the Engineering and Physical Sciences Research Council (EPSRC grants EP/L015226/1 and EP/S023232/1) through a studentship. Animal experiments were supported by a Cancer Research UK grant [C48390/A21153] to GOF. The authors received further support from the National Institute for Health Research (NIHR) Biomedical Research Centre based at Guy's and St Thomas' NHS Foundation Trust and King's College London; and the Wellcome/EPSRC Centre for Medical Engineering at King's College London [WT 203148/Z/16/Z]. This research was funded in whole, or in part, by the Wellcome Trust [WT203148/Z/16/Z]. For the purpose of open access, the author has applied a CC BY public copyright licence to any Author Accepted Manuscript version arising from this submission. The views expressed are those of the authors and not necessarily those of the NIHR, the National Health Service or the Department of Health. Dr Fahad Al-Salemeel is acknowledged for technical assistance for in vivo experiments.

Appendix A. Supplementary material

Supplementary data to this article can be found online at https://doi.org/10.1016/j.bmc.2022.117097.

References

1 Neidle S. Quadruplex nucleic acids as targets for anticancer therapeutics. *Nat Rev Chem*. 2017;1:0041.
2 Hansel-Hertsch R, Di Antonio M, Balasubramanian S. DNA G-quadruplexes in the human genome: detection, functions and therapeutic potential. *Nat Rev Mol Cell Biol*. 2017;18:279–284.
3 Varshney D, Spiegel J, Zyner K, Tannahill D, Balasubramanian S. The regulation and functions of DNA and RNA G-quadruplexes. *Nat Rev Mol Cell Biol*. 2020;21:459–474.
4 Paeschke K, Burkovics P. Mgs1 function at G-quadruplex structures during DNA replication. *Curr Genet*. 2021;67:225–230.
5 Neidle S. Challenges in developing small-molecule quadruplex therapeutics. *Annu Rep Med Chem*. 2020;54:517–546.
6 Chaudhuri R, Bhattacharya S, Dash J, Bhattacharya S. Recent update on targeting c-MYC G-quadruplexes by small molecules for anticancer therapeutics. *J Med Chem*. 2021;64:42–70.
7 Ruggiero E, Richter SN. G-quadruplexes and G-quadruplex ligands: targets and tools in antiviral therapy. *Nucl Acids Res*. 2018;46:3270–3283.
8 Asamitsu S, Bando T, Sugiyama H. Ligand design to acquire specificity to intended G-quadruplex structures. *Chem Eur J*. 2019;25:417–430.
9 Dhamodharan V, Pradeepkumar PI. Specific recognition of promoter G-quadruplex DNAs by small molecule ligands and light-up probes. *ACS Chem Biol*. 2019;14:2102–2114.
10 Savva L, Georgiades SN. Recent developments in small-molecule ligands of medicinal relevance for harnessing the anticancer potential of G-quadruplexes. *Molecules*. 2021;26:841.
11 Santos T, Salgado GF, Cabrita EJ, Cruz C. G-quadruplexes and their ligands: biophysical methods to unravel G-quadruplex/ligand interactions. *Pharmaceuticals*. 2021;14:769.
12 Largy E, Granzhan A, Hamon F, Verga D, Teulade-Fichou M-P. Visualizing the quadruplex: from fluorescent ligands to light-up probes. *Top Curr Chem*. 2013;330:111–178.
13 Monchaud D. Quadruplex detection in human cells. *Annu Rep Med Chem*. 2020;54:113–140.
14 Vummidi BR, Alzeer J, Luedtke NW. Fluorescent probes for G-quadruplex structures. *ChemBioChem*. 2013;14:540–558.
15 Raguseo F, Chowdhury S, Minard A, Di Antonio M. Chemical-biology approaches to probe DNA and RNA G-quadruplex structures in the genome. *Chem Commun*. 2020;56:1317–1324.
16 Di Antonio M, Ponjavic A, Radzevicius A, et al. Single-molecule visualization of DNA G-quadruplex formation in live cells. *Nat Chem*. 2020;12:832–837.
17 Shivalingam A, Izquierdo MA, Marois AL, et al. The interactions between a small molecule and G-quadruplexes are visualized by fluorescence lifetime imaging microscopy. *Nat Commun*. 2015;6:8178.
18 Summers PA, Lewis BW, Gonzalez-Garcia J, et al. Visualising G-quadruplex DNA dynamics in live cells by fluorescence lifetime imaging microscopy. *Nat Commun*. 2021;12:162.
19 Kench T, Vilar R. Metal complexes as G-quadruplex binders. *Annu Rep Med Chem*. 2020;54:485–515.
20 Georgiades SN, Abd Karim NH, Suntharalingam K, Vilar R. Interaction of metal complexes with G-quadruplex DNA. *Angew Chem Int Ed*. 2010;49:4020–4034.
21 Reed JE, Arnal AA, Neidle S, Vilar R. Stabilization of G-quadruplex DNA and inhibition of telomerase activity by square-planar nickel(II) complexes. *J Am Chem Soc*. 2006;128:5992–5993.
22 Arola-Arnal A, Benet-Buchholz J, Neidle S, Vilar R. Effects of metal coordination geometry on stabilization of human telomeric quadruplex DNA by square-planar and square-pyramidal metal complexes. *Inorg Chem*. 2008;47:11910–11919.
23 Wu P, Ma D-L, Leung C-H, et al. Stabilization of G-quadruplex DNA with platinum(II) schiff base complexes: luminescent probe and down-regulation of c-myc oncogene expression. *Chem Eur J*. 2009;15:13008–13021.
24 Campbell NH, Karim NHA, Parkinson GN, et al. Molecular basis of structure-activity relationships between salphen metal complexes and human telomeric DNA quadruplexes. *J Med Chem*. 2012;55:209–222.
25 Lecarme L, Prado E, Rache AD, Nicolau-Travers M-L, Bonnet R. Heyden AvD, Philouze C, Gomez D, Mergny J-L, Jamet H, Defrancq E, Jarjayes O, Thomas F, Interaction of Polycationic Ni(II)-Salophen Complexes with G-Quadruplex DNA. *Inorg Chem*. 2014;53:12519–12531.
26 Terenzi A, Bonsignore R, Spinello A, et al. Selective G-quadruplex stabilizers: Schiff-base metal complexes with anticancer activity. *RSC Adv*. 2014;4:33245–33256.
27 Davis KJ, Richardson C, Beck JL, et al. Synthesis and characterisation of nickel Schiff base complexes containing the meso-1,2-diphenylethylenediamine moiety: selective interactions with a tetramolecular DNA quadruplex. *Dalton Trans*. 2015;44:3136–3150.
28 Ali A, Kamra M, Roy S, Muniyappa K, Bhattacharya S. Novel oligopyrrole carboxamide based nickel(II) and palladium(II) salens, their targeting of human G-quadruplex DNA, and selective cancer cell toxicity. *Chem- Asian J*. 2016;11:2542–2554.
29 Zhou C-Q, Liao T-C, Li Z-Q, et al. Dinickel-salphen complexes as binders of human telomeric dimeric G-quadruplexes. *Chem- Eur J*. 2017;23:4713–4722.
30 Bandeira S, Gonzalez-Garcia J, Pensa E, Albrecht T, Vilar R. A redox-activated G-quadruplex DNA binder based on a platinum(IV)-salphen complex. *Angew Chem Int Ed*. 2018;57:310–313.
31 Ruehl CL, Lim AHM, Kench T, Mann DJ, Vilar R. An cctahedral cobalt(III) complex with axial NH3 ligands that templates and selectively stabilises G-quadruplex DNA. *Chem - Eur J*. 2019;25:9691–9700.
32 Abd Karim NH, Mendoza O, Shivalingam A, et al. Salphen metal complexes as tunable G-quadruplex binders and optical probes. *RSC Adv*. 2014;4:3355–3363.
33 Kench T, Summers PA, Kuimova MK, Lewis JEM, Vilar R. Rotaxanes as cages to control DNA binding, cytotoxicity, and cellular uptake of a small molecule**. *Angew Chem Int Ed*. 2021;60:10928–10934.
34 Banerjee S, Capper MS, Clarkson GJ, Huang H, Sadler PJ. Dual-action platinum(II) Schiff base complexes: photocytotoxicity and cellular imaging. *Polyhedron*. 2019;172:157–166.
35 Marchetti C, Zyner KG, Ohnmacht SA, et al. Targeting multiple effector pathways in pancreatic ductal adenocarcinoma with a G-quadruplex-binding small molecule. *J Med Chem*. 2018;61:2500–2517.
36 Ohnmacht SA, Marchetti C, Gunaratnam M, et al. A G-quadruplex-binding compound showing anti-tumour activity in an in vivo model for pancreatic cancer. *Sci Rep*. 2015;5:11385.
37 Khosravifarsani M, Ait-Mohand S, Paquette B, Sanche L, Guerin B. High cytotoxic effect by combining copper-64 with a NOTA-terpyridine platinum conjugate. *J Med Chem*. 2021;64:6765–6776.
38 Cormier SA, Taranova AG, Bedient C, et al. Pivotal Advance: Eosinophil infiltration of solid tumors is an early and persistent inflammatory host response. *J Leukoc Biol*. 2006;79:1131–1139.
39 Xie D, Jing J, Cai YB, Tang J, Chen JJ, Zhang JL. Construction of an orthogonal ZnSalen/Salophen library as a colour palette for one-and two-photon live cell imaging. *Chem Sci*. 2014;5:2318–2327.
40 Stootman FH, Fisher DM, Rodger A, Aldrich-Wright JR. Improved curve fitting procedures to determine equilibrium binding constants. *Analyst*. 2006;131:1145–1151.
41 Thordarson P. Determining association constants from titration experiments in supramolecular chemistry. *Chem Soc Rev*. 2011;40:1305–1323.
42 Otsu N, Threshold A. Selection method from gray-level histograms. *IEEE Trans Syst Man Cybern*. 1979;9:62–66.